Effect of oxygen on corrosion of an alumina-forming duplex steel in static liquid lead-bismuth eutectic at 550 °C

Lingzhi Chen [a], Valentyn Tsisar [b], Man Wang [c], Carsten Schroer [b], Zhangjian Zhou [a,*]

[a] *University of Science and Technology Beijing, School of Material Science and Engineering, Beijing, 100083, China*
[b] *Karlsruhe Institute of Technology (KIT), Institute for Applied Materials - Applied Materials Physics, Karlsruhe, 76344, Germany*
[c] *Beijing University of Technology, College of Materials Science and Engineering, Beijing, 100124, China*

ARTICLE INFO

ABSTRACT

Corrosion in static liquid lead–bismuth eutectic (LBE) with varying oxygen content is investigated at 550 °C on an alumina-forming duplex steel which contains both austenite and ferrite phases. The duration of the tests is about 1000 h. For oxygen concentration ranging from 10^{-12} to 10^{-8} % by mass, the steel shows preferential nickel dissolution and LBE penetration. The degradation of the ferrite is delayed in contrast to the austenitic part of the duplex microstructure. At 10^{-6} % oxygen, the steel is protected from LBE attack due to the formation of a thin oxide layer rich in aluminum. The precipitation of NiAl in the steel does not compromise the formation of Al-rich oxide at this oxygen concentration.

1. Introduction

To solve the long-term energy demand and carbon emission problems, clean and sustainable energy such as advanced nuclear and solar energy have attracted worldwide attention [1]. Liquid lead and its alloys, e.g. the lead–bismuth eutectic (LBE), show excellent high-temperature thermal performance and nuclear physical properties, thus are very suitable for cooling the core of a nuclear reactor. For example, LBE is an important coolant for fast reactors, and liquid Pb-Li alloy is promising for breeding blanket application in fusion reactors [2]. They are also considered as promising heat storage media in concentrating solar power systems [3,4].

Compared with high-temperature water, liquid lead-based alloys have much higher capacity to dissolve solid metals. Significant dissolution of the main elements of steels, namely Ni, Cr, and Fe, have been found in liquid lead and particularly in LBE [5]. Austenitic steels such as 316 L and 15 15Ti have been selected as candidate materials for the cladding tubes in liquid-metal cooled reactors due to their good high-temperature strength, ductility and machinability. However, Ni shows clearly higher solubility in liquid lead than Cr and Fe, therefore, austenitic steels with high Ni content usually suffer from more severe corrosion in liquid lead alloys compared with ferritic steels. The development of new steel grades with enhanced corrosion resistance in liquid lead alloys is one of the key issues for their application to lead-cooled energy systems.

Recently, a number of materials including austenitic and ferritic/martensitic steels, as well as corresponding oxide dispersion strengthened grades have been tested in liquid lead-based alloys [6–9]. The obtained results show that proper selection of minor alloying elements combined with suitable control of oxygen dissolved in the liquid metal is an efficient way to increase corrosion resistance of steels, as a dense, thin protective oxide layer may form on the steel surface, minimizing the dissolution of the substrate. The success of oxygen addition, however, does not always meet the intuitive expectation: For example, Si-alloyed steels show generally improved corrosion resistance in LBE due to a Si-rich oxide layer inside the scale formed on the surface [10], but local steel dissolution may be observed especially at higher concentration of dissolved oxygen [11]. Hence, it is very important to control the oxygen content of the liquid metal accurately, based on the investigation of the relationship between alloy composition and appropriate oxygen content.

Similar to Si, Al generally takes a beneficial effect on steel oxidation [12,13]. Furthermore, addition of Al to austenitic steels increases the high-temperature strength. Both is exploited through the so-called alumina-forming austenitic (AFA) stainless steels, developed first by the Oak Ridge National Laboratory in recent years [14–16]. The AFA steels show good creep performance in the temperature range from 600 to 900 °C and oxidation resistance in dry and humid air. Al_2O_3 scales formed on

---

the surface of AFA steels are more stable in high-temperature water environment than the Cr_2O_3 scales typically found on other austenitic grades [17,18].

In contrast to the severe corrosion of traditional austenitic steels in liquid lead alloys [19,20], the performance of AFA steels in oxygen-containing liquid lead is promising based on preliminary works [21,22]. However, the related studies are still rather limited, more works are necessary to collect sufficient data and especially establish the relationship between oxygen content and formation of a protective alumina scale.

Al is a strong ferrite-forming element so that AFA steels tend to develop a duplex structure if the Al content is high in proportion to the amount of Ni and Cr in the steel. Another phase forms by precipitation of stable NiAl in the course of aging at elevated temperature typically below 1000 °C. NiAl more easily precipitates in the ferrite in comparison to the austenitic phase [23]. The ferritic phase usually contains more Al and Cr and less Ni than the austenitic phase so that, if favorable oxidation (Al, Cr) and undesirable dissolution (Ni) were merely linked to the chemical composition, the ferrite would be less prone to corrosion caused by oxygen-containing liquid lead alloys than the austenite. NiAl accumulates both Ni and Al in the steel with potentially delaying effect on the dissolution of these elements if a protective oxide scale on the steel surface is not or not yet present. However, Al supply for the establishment of an alumina layer might equally be delayed in comparison to same amount of Al in solid solution in either austenite or ferrite. Thus, increasing the Al content in typical AFA steels not only renders the formation of protective alumina more likely, but involves additional effects of the resulting duplex microstructure and enhanced precipitation of NiAl that deserve closer examination.

The presented study aims at screening the performance of Fe-18Ni-16Cr-4Al-2Mo-0.4Nb steel in static LBE at 550 °C as a function of oxygen concentration between 10^{-12} and 10^{-6} % by mass. The high addition of Al in comparison to typical AFA steels makes the microstructure of this material austenitic/ferritic duplex in the as-produced state [23]. The post-test examinations primarily focus on the influence of the concentration of dissolved oxygen, but also address the effect of the austenitic/ferritic duplex structure and NiAl on observed corrosion.

2. Experimental

2.1. Materials

The investigated AFA steel with a nominal composition of Fe-18Ni-16Cr-4Al-2Mo-0.4Nb was fabricated by vacuum induction melting. The ingot was forged with a forging ratio of 3:1, then subjected to hot rolling at 1150 ℃ with a total reduction of 80 %. The detailed fabrication route can be found elsewhere [23].

The actual chemical composition measured by inductively coupled plasma optical emission spectrometry (ICP-OES) is listed in Table 1. According to thermodynamic calculation, the designed AFA steel forms both austenitic and ferritic phases. Electron backscatter diffraction (EBSD) in the scanning electron microscope (SEM) as well as the results from energy-dispersive X-ray spectrometry (EDS) verify the dual phase microstructure (Fig. 1a). Based on the EBSD analysis, the material consists of 78 % (by volume) austenitic phase (red-colored area in Fig. 1b) and 22 % ferrite (blue-colored area in Fig. 1b), which is consistent with thermodynamic calculation by software of JMatPro with stainless steel database. The calculated percentage of austenite and ferrite phase is 78.8 % and 21.2 %, respectively. According to the repeatedly performed EDS analyses, Ni, Cr and Al are about 19, 15.5 and

3.6 % by mass, respectively, in the austenitic phase, while the ferrite contains less Ni, more Cr and Al (Fig. 1a). The ferritic phase contains NiAl precipitates already with sizes of tens of nm in the as-fabricated state as seen in the upper right picture in Fig. 1a, which also was reported in our previous work [23].

2.2. Corrosion test

Cylindrical samples with nominal dimensions of Ø8 mm × 15 mm were cut from the rolled plate and provided with a central borehole. The long axis of the cylinders is parallel to the rolling direction. The surface of the samples was finished by fine-turning, cleaned and degreased in acetone. The actual diameter of the samples was measured in a laser micrometer with reading accuracy of 0.1 μm.

Fig. 2 shows the device used for the exposure test in liquid LBE. The corrosion samples are mounted to a Mo rod and immersed in 200 mL static LBE. The LBE is contained in an alumina crucible. Two pairs of thermocouple and associated oxygen sensor (with Pt/air reference electrode) monitor the temperature and dissolved oxygen concentration in two positions inside the crucible: (1) in the horizontal plane that corresponds to the center of the sample holder, and (2) 30 mm above this plane, i.e. close to the liquid metal surface. The output of the thermocouple and oxygen sensor in the vicinity of the samples is taken as representative of the exposure conditions, and is utilized as the reference for automated oxygen control. The second pair of sensors provides an indication of the uniformity of temperature and dissolved oxygen in the LBE volume as well as some information with regards to the oxygen transfer process. The oxygen concentration in the liquid LBE is controlled using a flowing gas mixture of Ar, Ar-5 % H_2 (% by volume), and synthetic air, which is introduced above the liquid metal surface. 10^{-11} to 10^{-12} % as specified for the test at lowest concentration of dissolved oxygen resulted for guiding a continuous Ar–5 % H_2 flow over the LBE surface.

The dissolved oxygen concentration c_o is calculated from the sensor output as [24]:

$$\log c_O \quad -3.2837 + 6949.8/\,T - 10{,}080 \times (U - U_{th})/\,T \tag{1}$$

where, c_O is the concentration of dissolved oxygen in % by mass, T denotes the temperature in K, U is the sensor output in V. U_{th} represents a thermoelectric voltage effective in the measurement. Thermoelectric voltage arises from the Mo holder being part of the measuring circuit, whereas other electric leads such as the autoclave and the electric lead of the reference electrode of the oxygen sensors consist of stainless steel. Estimating U_{th} for the experimental set-up at 550 °C temperature of the LBE results in 7 mV [24].

Four tests were performed at 550 °C and different c_O, in which the steel of interest in the presented study was one out of three Fe–Ni–Cr–Al materials exposed simultaneously to the liquid LBE. The exposure time each was around 1000 h.

Table 2 shows the identifiers of the four tested samples and the corresponding nominal oxygen content in LBE. The indicated testing temperature (Thermocouple 1 in Fig. 2) always was 550 (+/–2) °C. The temperature difference between samples and liquid-metal surface as revealed by comparison with the output of Thermocouple 2 varied between about 1 °C (in the experiment at nominally 10^{-6} % dissolved oxygen) and 10 °C (experiment at nominally 10^{-11} to 10^{-12} % oxygen), which gave rise to respective thermal convection in the liquid-metal volume. The actual oxygen concentrations calculated from the signal of the sensor that resides close to the samples (Oxygen sensor 1 in Fig. 2)

Table 1
Chemical composition of the investigated steel (% by mass).

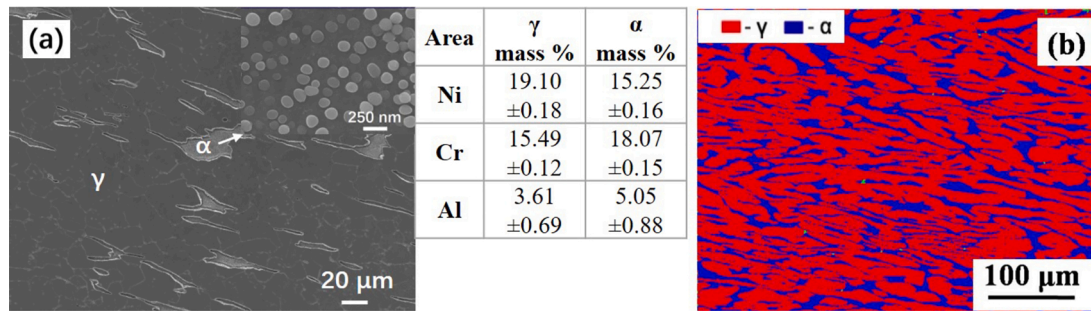| C	Al	Si	Cr	Mn	Mo	Ni	Nb	Fe
0.014	4.120	0.365	15.501	0.071	2.003	17.803	0.391	Balance

Fig. 1. (a) SEM micrograph and results from each four EDS analyses for the as-fabricated duplex steel. The insert picture magnifies the of α area; (b) EBSD phase map.
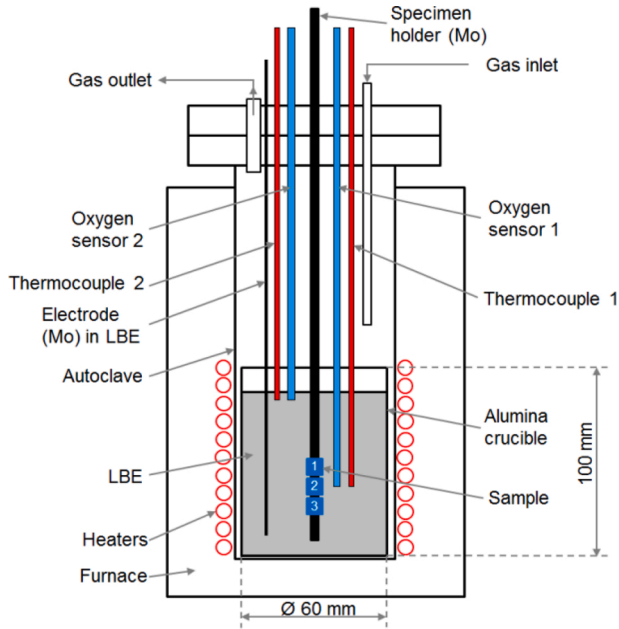

Fig. 2. Schematic illustration of the device for LBE corrosion tests.

Table 2
Sample identifiers, corresponding exposure times and nominal oxygen contents.

Identifier	Actual exposure time (h)	c_O (% by mass)
D-12O	1005	10^{-11}-10^{-12}
D-9O	930	10^{-9}
D-8O	1158	10^{-8}
D-6O	1085	10^{-6}

are shown in Fig. 3. Accordingly, the oxygen concentration close to the samples was fairly stable during the tests on the samples D-9O, D-8O or D-6O. For the sample D-12O, the dissolved oxygen concentration close to the sample holder gradually decreased to 10^{-12} %, and was between 10^{-11} and 10^{-12} % for the best part of the experiment. Oxygen concentration close to the LBE surface was by 2–3 orders of magnitude higher, implying that the very low concentration at the sample holder primarily resulted from oxygen consumption by the samples, sample holder or elements dissolving elements from the samples. In the steady state of the experiment at nominally 10^{-9} % dissolved oxygen, the concentration at the LBE surface was about a quarter order of magnitude higher than close to the samples, which is indicative of the oxygen gradient required for balancing oxygen consumption under these conditions. During the tests at nominally 10^{-8} or 10^{-6} % dissolved oxygen, the difference in oxygen concentration indicated by the two sensors was within the expected accuracy ($+/-$ 10 % in calculated concentration at 550 °C) of the type of sensor utilized [24].
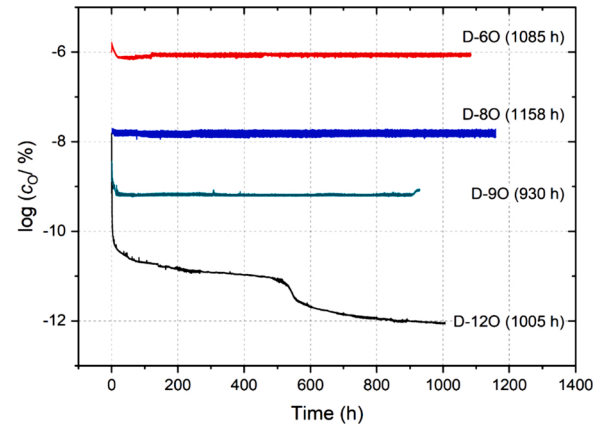

Fig. 3. Dissolved oxygen concentration c_O as a function of exposure time for the tests performed in liquid LBE.

At 550 °C, Al and Cr are likely to oxidize at all oxygen concentrations of interest, whereas $> 10^{-9}$ % by mass are required for formation of binary Fe oxides. Oxidation of Ni and the constituent parts of LBE, i.e. Pb and Bi, cannot occur under the conditions of the tests [24,25].

2.3. Post-test examination

After the corrosion test, the samples were cut in half, perpendicularly with respect to the long cylinder axis, and metallographic cross sections prepared using standard metallographic techniques. Cold mounting resin was used in order to avoid re-melting of the adherent LBE that was maintained for the cross-section analysis.

In the light optical microscope (LOM), micrographs were taken at 100-fold magnification along the whole circumference and stitched together using image processing software, so as to document the distribution of corrosion along the cross-section circumference. The corrosion depth was assessed at 1000-fold magnification directly in the LOM for 24 positions uniformly distributed along the circumference of the samples and the average calculated. In the case of local corrosion, those of the points selected for measurement that show practically zero corrosion depth were not considered in the calculation of the average corrosion depth. If not already included in the systematic assessment, another measurement of the maximum of local degradation was performed. The microstructure of observed corrosion scales was investigated in the SEM (LEO-1450 and JEOL JSM6400) equipped with EDS.

In order to characterize the thin oxide scale that formed, a transmission electron microscope (TEM) sample containing the area of interest was prepared by the in-situ lift-out technique. For this purpose, a focused ion beam (FIB) was used, or, more precisely, an integrated dual-beam FIB/SEM system incorporated with a versatile nanomanipulator (tungsten probe, Zeiss Auriga). The FIB/SEM system with a resolution of 2 nm was operated at an accelerating voltage of 30 kV. Pt was deposited

on the surface of the sample and Ga^+ ions were used to cut the cross section of the sample. Then it was lifted out and attached to a Cu support grid for TEM observation. TEM microstructures were investigated using bright-field (BF) imaging at 200 kV (Titan themis G2 60–300 equipped with Tecnai G2 F30 S-TWIN EDS).

3. Results

3.1. LOM

Fig. 4 shows the circumference of the cross sections prepared from samples after exposure to LBE at different c_O. The circles represent the original position of the sample surface reconstructed with the aid of the initial diameter determined before the tests. Degradation caused by liquid metal attack is evident for the samples D-12O, D-9O and D-8O, while D-6O does not show any remarkable attack.

Fig. 5 shows micrographs of the typical corrosion scales on the tested samples. The duplex microstructure is apparent for all depicted cross sections, as the austenitic phase appears slightly brighter than the ferrite in the micrographs. Scales observed on D-12O, D-9O and D-8O are characteristic for dissolution by LBE or, more precisely, the selective leaching of steel elements accompanied by penetration of the liquid metal [26–28]. Solidified LBE occasionally adheres to the sample surface. For D-9O or D-8O, observed scales are thin in comparison with D-12O. In the LOM, no corrosion scale is found for D-6O, i.e. after exposure at 10^{-6} % oxygen, the steel is obviously protected from otherwise occurring dissolution.

Fig. 6 presents the results from measuring the scale thickness or corrosion depth, the average from up to 24 measurements in each cross section as well as the maximum attack observed. Furthermore, the percentage of protected surface area (stars, right axis) is indicated. Sample D-12O shows the highest average and maximum corrosion depth, namely 179 and 350 µm, respectively. 3 out of the 24 sites evaluated do not show any sign of corrosion in the LOM so that the percentage of surface protected from liquid metal attack is estimated 12.5 %. In the case of D-6O, liquid metal attack in the form of selective leaching is not observed at all in the examined cross section, corresponding to 100 % protected surface. A thin oxide layer that is analysed in detail in Section 3.3 suppresses noticeable dissolution. While the percentage of protected surface area monotonously increases with dissolved oxygen increasing from 10^{-12} % to 10^{-6} %, the corrosion depth
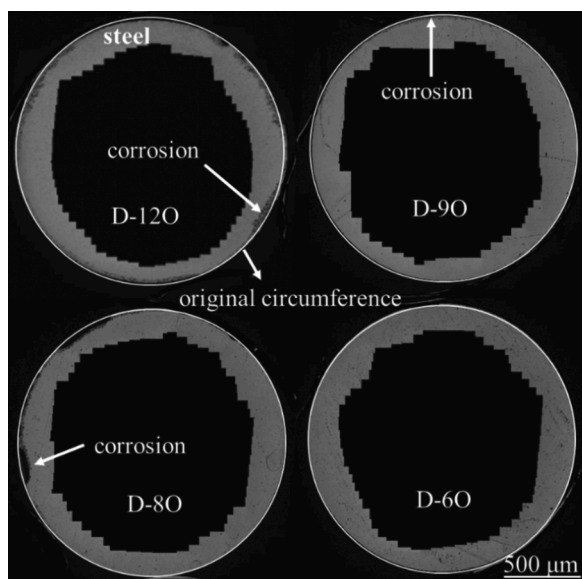
exhibits a local minimum at 10^{-9} %. The material loss caused by oxidation (D-6O) is practically zero.

3.2. SEM

Fig. 7 shows SEM micrographs of the typical corrosion scale on D-8O, D-9O and D-12O. Images are sorted by (from a to c) increasing magnification. Pb and Bi with relatively high atomic mass appear rather bright in the images, implying significant penetration of LBE into the matrix. Fig. 7a taken from the cross section of the sample D-8O exemplifies locally heavy attack and the transition to areas having experienced slighter corrosion. The corrosion pit primarily contains solidified LBE, and a minimum of steel remnants that are characteristic for the selective leaching of elements. The material has largely dissolved. Fig. 7b corresponds to the maximum of corrosion observed in the cross section evaluated for the sample D-12O (arrow). The steel remnants dominate the inner part of the penetrated zone, solidified LBE dominates the near-surface quarter. Comparatively slight attack with high percentage of steel remnants in the entire corrosion zone is generally observed in the sample D-9O (Fig. 7c) but also between the corrosion pits in D-8O. The high magnification micrograph presented as Fig. 7c further implies that one of the phases in the duplex structure of the tested steel is less affected by the penetration of Pb and Bi. In non-penetrated areas (ferrite), Ni depletion is comparatively slight.

Fig. 8 shows EDS mapping results for the rectangular area indicated in Fig. 7a. In the part heavily attacked by LBE, the leaching of steel elements is already in an advanced stage, Fe and especially Ni and Al lag behind in the few remnants of the steel. The latter suggest Ni-rich aluminide. Closer to the unaffected steel, where leaching has not yet advanced this far, two types of grains with different contents of Fe, Cr and Ni are reminiscent of the original duplex structure. Relatively Cr-rich grains also contain Ni and Al. Their interface with LBE that penetrated the corrosion scale seems to be a prefereed place of formation of the Ni- and Al-rich phase (titled arrows in Fig. 8). The produced oxygen map is not clear enough for deciding on whether oxidation is involved, however, formation of ternary Ni-Al oxide can be excluded in view of the oxygen concentration in LBE during the test [25]. The other type of grains primarily consists of Fe and Al, whereas Ni and Cr concentrations are comparatively low. Penetrated LBE seperates these domains from the especially Cr-rich grains (horizontal arrows in Fig. 8). Clearly dominant Fe content and high Cr concentration, respectively, imply that both types of grains are ferrite. Low Ni and reduced Cr content are typical for ferrite formed by austenite transformation in connection with selective leaching of this elements [26].

Fig. 9 shows a part of the scale on D-12O at relatively high magnification together with the results from EDS line-scan analysis. Especially Ni but also Cr are depleted in the corrosion scale in comparison with the unaffected steel, whereas the Fe content in the steel remnants has increased. Bi and Pb penetrate into the space that opens because of the loss of steel elements.

Fig. 10 shows the EDS elemental mapping at the transition between depletion zone and steel in D-9O, which suggests selective corrosion and penetration along phase boundaries and of the austenitic phase in the duplex steel structure. There is hardly any attack of the ferritic phase beyond a few microns from the original material surface. It is obvious from the EDS mapping results that the content of Ni in the corroded austenite phase is greatly reduced, and the austenite is ferritized (as shown by $\gamma \rightarrow \alpha$ in the figure). This observation on sample D-9O generally applies also to selective leaching in samples D-12O and D-8O. Further EDS point analyses show that after the corrosion test, the composition (% by mass) in areas corresponding to the original γ and α phase are Fe-6Ni-2Cr-13Al and Fe-14Ni-19Cr-9Al, respectively. As suggested when evaluating Fig. 8, the ferrite (formed by ferritization of austenite) is poor in Cr as a result of selective leaching of Ni and Cr from the γ-phase in the duplex steel.

The oxide scale anticipated where LBE apparently has not taken any

Fig. 4. Complete circumference of the cross sections investigated after the tests reproduced by stitching of LOM images.
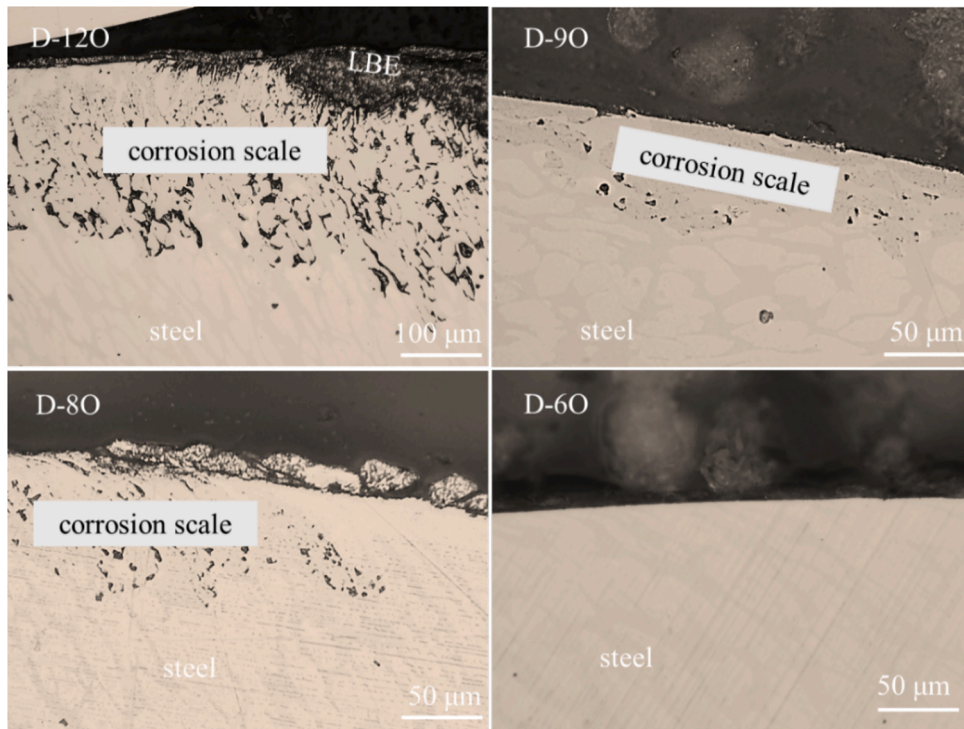
Fig. 5. Corrosion scales locally found in the cross sections of D-12O, D-9O and D-8O, respectively, that are not observed for D-6O. Note the lower magnification for D-12O.
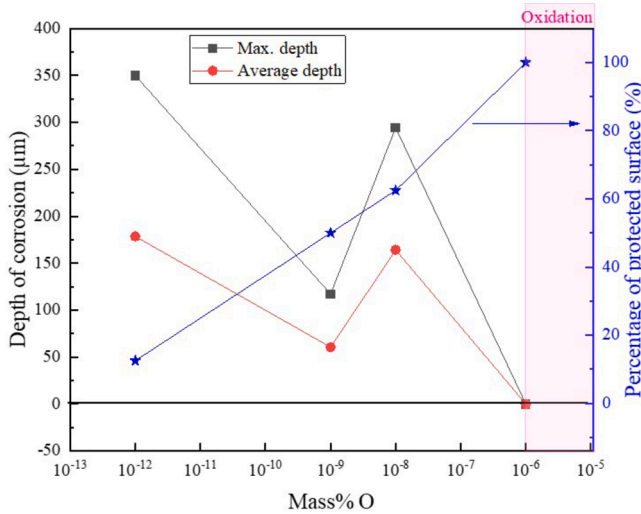

Fig. 6. Results from quantifying corrosion after exposure for order of 1000 h to static LBE at 550 °C as a function of dissolved oxygen concentration.

effect on the tested steel is too thin to be resolved in the SEM. In the example shown in Fig. 11, the protected surface corresponds to a ferritic domain in the duplex steel, most likely with Ni-rich aluminide near the surface. The peculiar shape of the austenite grain following next in the direction towards the bulk of the steel suggests a near-surface γ/α transition along with or preceding the development of the protective scale. However, it should be noted that SEM/EDS occasionally indicates austenite immediately at the protected surface.

3.3. TEM

The results from examining the near-surface portion of the sample D-6O in the TEM are introduced in Figs. 12 and 13. The TEM/EDS elemental maps in Fig. 12 indicate a 6 8 μm thick near surface zone characterized by nano-sized Ni- and Al-rich particles dispersed in the matrix. Additional EDS point analysis suggest 50 % (by mass) Ni and 33 % Al for the Ni- and Al- rich particles, along with 3.4 % Cr. The surrounding steel phase contains only 2.0 and 0.08 % Ni and Al, respectively, but 21 % Cr. The grain or part of a grain following in the direction towards the bulk of the steel is austenite as revealed by the high content of Ni and low content of Cr, as well as the absence of spherical NiAl particles. The distribution of elements in the dispersed Ni- and Al-rich particles zone as well as surface oxide scale enriched in Cr, Al and
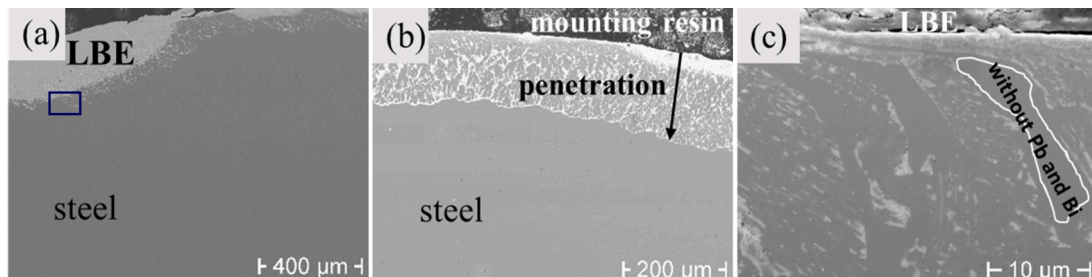

Fig. 7. Near-surface portion of the cross sections of samples (a) D-8O, (b) D-12O, and (c) D-9O, the rectangular areas marked in picture (a) will be analyzed in Fig. 8.
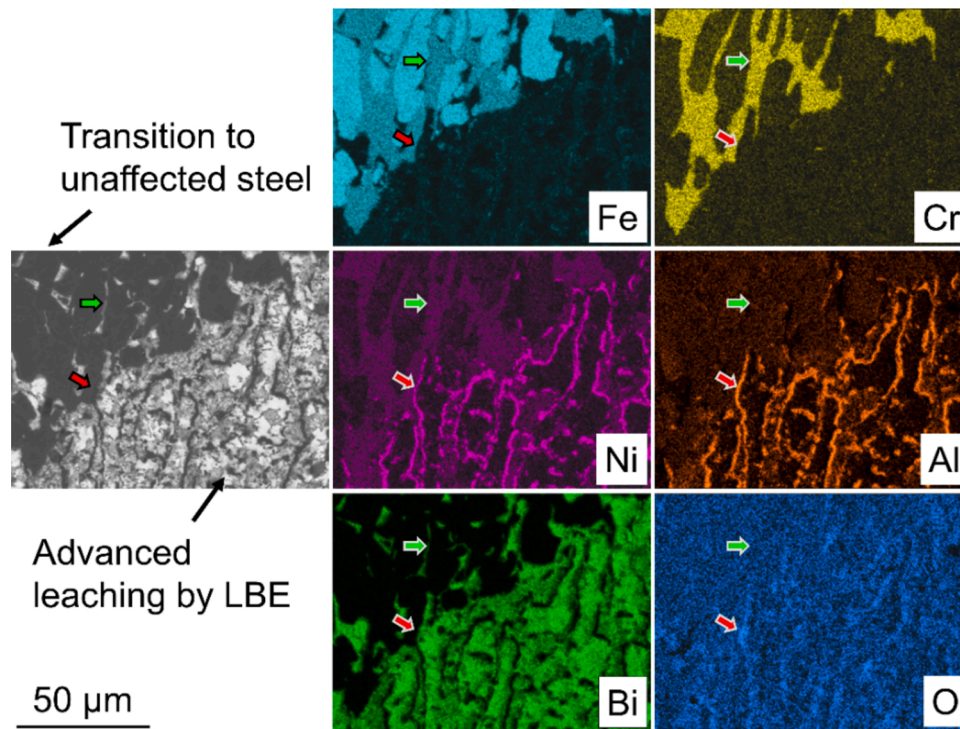
Fig. 8. Results from EDS element mapping inside the corrosion scale on D-8O. The Bi map is also representative for the qualitative distribution of Pb. The two sets of arrows have been added for better orientation.
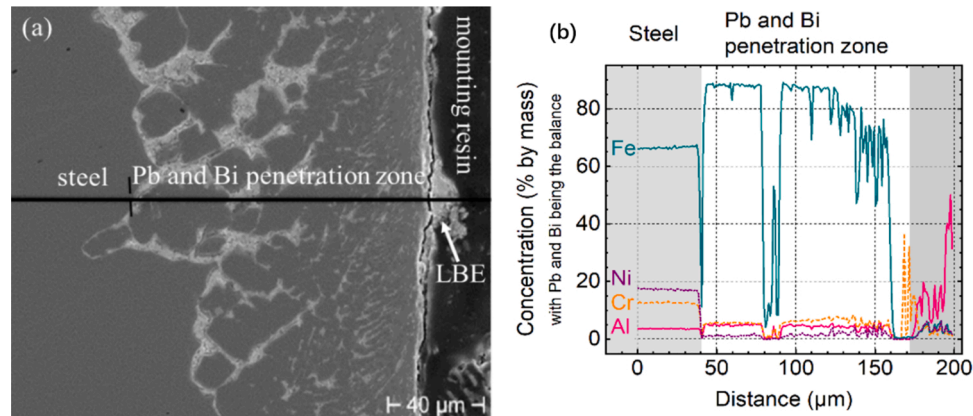

Fig. 9. (a) SEM micrograph (cross section) of the corrosion layer on D-12O together with (b) the results of EDS line scan across this layer, namely the concentration of Fe, Ni, Cr and Al, respectively, with Pb and Bi being the balance.

oxygen are shown at higher magnification in Fig. 13a.

Fig. 13b and c focus on part immediately at the surface, especially the surface layers. Three layers are identified in Fig. 13b with the aid of the EDS line-scan presented in Fig. 13c. Although the recorded oxygen profile is not especially clear in this respect, the presence of oxide is non-ambiguous from the elemental maps in Fig. 13a. The thickness of the oxide scale formed by the three layers is < 200 nm. A thin LBE film adheres to the oxide scale surface. Information combined suggests: (1) Al-rich oxide at the interface with the steel; (2) an intermediate layer rich in Cr and Al; and (3) Fe- and Cr-rich oxide in contact with the adherent LBE. Especially the innermost, Al-rich layer is continuous.

4. Discussion

Similar to other steels, especially austenitic grades of the 316 family [19,20,22,26,27] or AFA [20,29], the interaction of the

alumina-forming duplex steel in oxygen-containing LBE at 550 °C is generally characterized by the competition between element dissolution and surface oxidation. Naturally, the concentration of oxygen dissolved in the liquid metal is a decisive factor. The observed trends in the qualitative and quantitative performance of the duplex steel are the same as for single phase AFA tested in the identical experiments [29].

At low oxygen concentration, namely 10^{-11} to 10^{-12} % by mass, the investigated steel primarily experiences solution-based corrosion. Missing evidence of corrosion for 12.5 % of the sites evaluated in the LOM (Figs. 4 and 6) indicates that parts of the surface are protected by a thin oxide scale. Precursors of this scale may already be present on the tested samples before exposure to LBE and some growth of oxide cannot be excluded for the initial phase, during which c_O decreases from 10^{-8} to 10^{-11}–10^{-12} % (Fig. 3). Dissolution is likely to start where the scale formed only imperfectly or failed after the decrease in c_O. At 10^{-9} %, oxides are generally more stable than at 10^{-11}–10^{-12} % dissolved
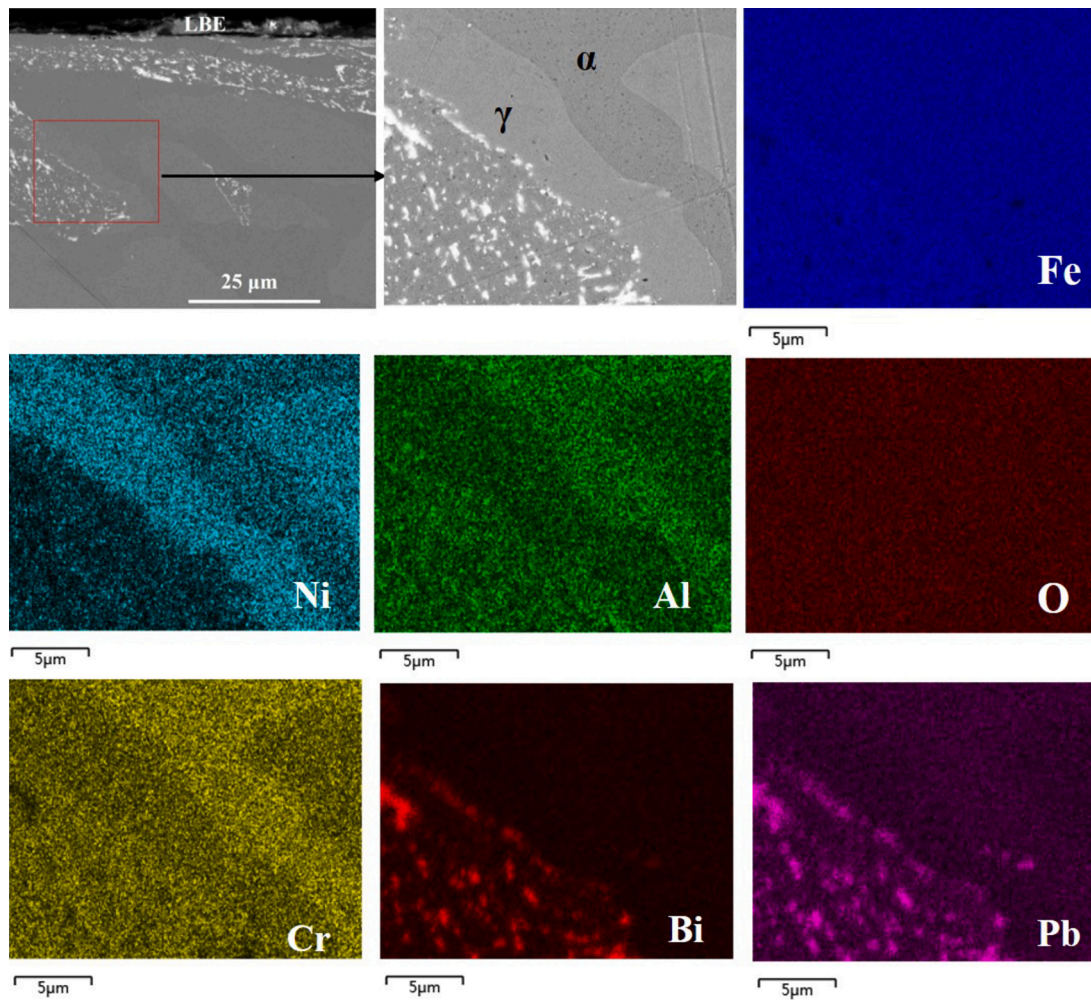
Fig. 10. EDS element mapping at the transition between depletion zone and steel in D-9O.

oxygen, so that the percentage of protected surface area increases in comparison to the lower oxygen content in LBE. The especially pronounced decrease of the maximum corrosion depth (Fig. 6) suggests prolonged incubation of dissolution, i.e. the selective leaching of steel elements. Fe is primarily retained in the remains of the steel that are penetrated by Pb and Bi (Fig. 10).

With further increase of dissolved oxygen to 10^{-8} %, the trend as to the percentage of protected surface persists, but the average and maximum corrosion depth observed approach the numbers for 10^{-11}–10^{-12} % rather than decrease in comparison to 10^{-9} % dissolved oxygen. The relatively low amount of steel remnants in the corrosion scale formed at 10^{-8}% oxygen (Fig. 7a) implies enhanced removal of Fe. The precipitation of Fe oxide in the liquid metal [26] is the most likely reason, especially if it is taken into account that Fe oxides become stable at around 10^{-8} % oxygen in LBE [25,30]. The associated increase in local material loss [26] explains the observed corrosion depth, whereas the incubation time of dissolution is likely to further increase with c_O increasing from 10^{-9} to 10^{-8} %.

At 10^{-6} % dissolved oxygen, a protective oxide scale fully establishes and persists for at least 1000 h. The originally austenitic and ferritic grains in the duplex steel are equally protected from dissolution in LBE or, more precisely, the selective leaching of steel elements. The TEM analysis of the oxide scale on ferrite shows that the innermost of three layers is likely to be alumina (Fig. 13). Cr enrichment in the other two layers corresponds to oxidation mechanisms applicable to Fe-Cr-Al alloys [31–33], in which Cr_2O_3 supports the formation of dense and slow-growing Al_2O_3. The amount of Fe–Al oxides is a minimum and

internal oxidation of Al avoided. Ni- and Al-rich aluminide, most likely NiAl that is present especially in the ferritic part of the duplex steel does apparently not bind too much Al for the protective scale to form even if some growth of these precipitates should occur at the exposure temperature of 550 °C. The Al map in Fig. 13a rather suggests the capability to dissolve and release Al, because NiAl particles that may also form close to the steel surface rarely touch the Al-rich oxide layer. For the austenitic grains, it seems possible that along with or preceding the establishment of a protective oxide scale, austenite transforms into ferrite (Figs. 11 and 12). This event may be triggered by intermittent leaching of Ni during the time the oxide layers need to develop, and supports the formation of a protective scale on originally austenitic grains because of faster element diffusion in ferrite [34,35]. The simultaneous precipitation of NiAl with mass density of about 6 g/cm^3 [36] from a steel phase with order of 8 g/cm^3 mass density is capable of reducing the porosity that otherwise results from the selective leaching of elements and, therefore, may avoid penetration of the liquid metal typically associated to the removal of steel elements. Especially after partial transition into ferrite, austenitic grains will oxidize similarly to the originally ferritic grains. Further Ni dissolution is unlikely once the oxide layers have established. While the presented study does not yet deliver clear proof for the γ/α transition in connection with oxidation in LBE, the latter may possibly be of relevance also for the oxidation mechanisms of single-phase AFA in the presence of liquid lead alloys.

The observed preference of selective leaching for the austenitic part of the duplex structure (Fig. 10) is probably linked to the higher concentration of highly soluble Ni. The higher content of oxide forming
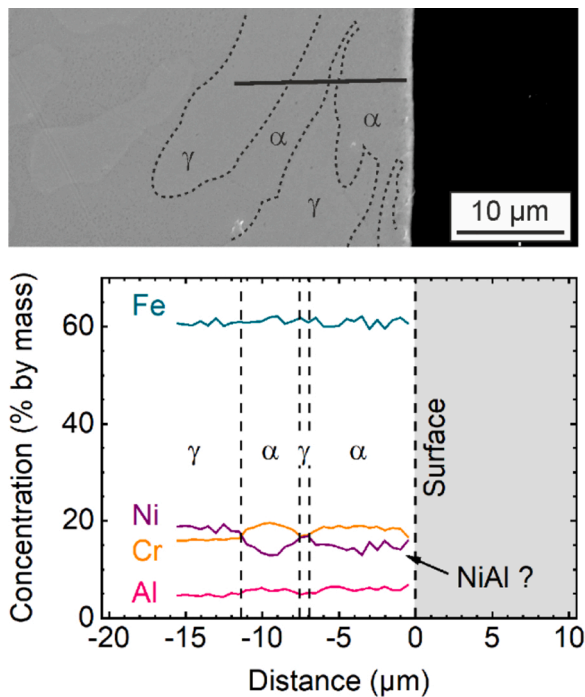
Fig. 11. Site apparently not affected by LBE corrosion in the cross section of D-8O and results from EDS analyses performed along the solid line indicated in the SEM image. The dotted lines retrace the contour of α or γ grains near the surface.

elements such as Cr and Al in the ferrite may also play a role that tends to increase in importance the higher the oxygen concentration in the liquid metal. In the early stage, the result of selective element leaching are two types of ferritic grains that differ in composition, of which the ones relatively poor in Cr and Ni form by transformation of the γ-phase. Where selective leaching has advanced comparatively far, accumulation of Ni and Al, possibly as intermetallic NiAl, is evident (Fig. 8).

5. Conclusions

The conclusions from investigating corrosion caused by static LBE at

550 °C and concentration of dissolved oxygen between 10^{-12} and 10^{-6} % by mass in alumina-forming duplex steel (Fe-18Ni-16Cr-4Al-2Mo-0.4Nb) are as follows:

1.) Performance of the duplex material as a function of dissolved oxygen demonstrates that at 550 °C, a significant concentration of oxygen (10^{-6} %) in LBE is required to form a stable protective oxide scale. The percentage of protected surface area gradually decrease for c_O decreasing from 10^{-6} to 10^{-12} %.
2.) Selective leaching starts where the surface is unprotected. The austenitic part of the duplex structure is generally consumed faster than the ferrite. Initially, the product of selective leaching are two types of ferritic grains that differ in their Ni and Cr content. Ni-aluminide is formed when selective leaching is far advanced. Observed corrosion depth increases for oxygen content increasing from 10^{-9} to 10^{-8} %, i.e. when Fe oxides become stable.
3.) The protective scale consists of oxides rich in chromium and aluminum, with aluminum-rich oxide especially at the interface with the steel. The latter forms despite prominent precipitation of Ni-rich aluminide. Indications found for a transition of austenite into ferrite in connection with the formation of the protective scale hint at a new aspect to be considered also for oxidation of single-phase AFA.

Data availability

The raw/processed data required to reproduce these findings cannot be shared at this time due to technical or time limitations, they will be made available on request.

CRediT authorship contribution statement

Lingzhi Chen: Conceptualization, Formal analysis, Methodology, Writing - original draft. **Valentyn Tsisar:** Investigation, Methodology, Writing - original draft. **Man Wang:** Investigation, Visualization, Formal analysis. **Carsten Schroer:** Supervision, Methodology, Writing - review & editing. **Zhangjian Zhou:** Supervision, Writing - review & editing, Project administration.
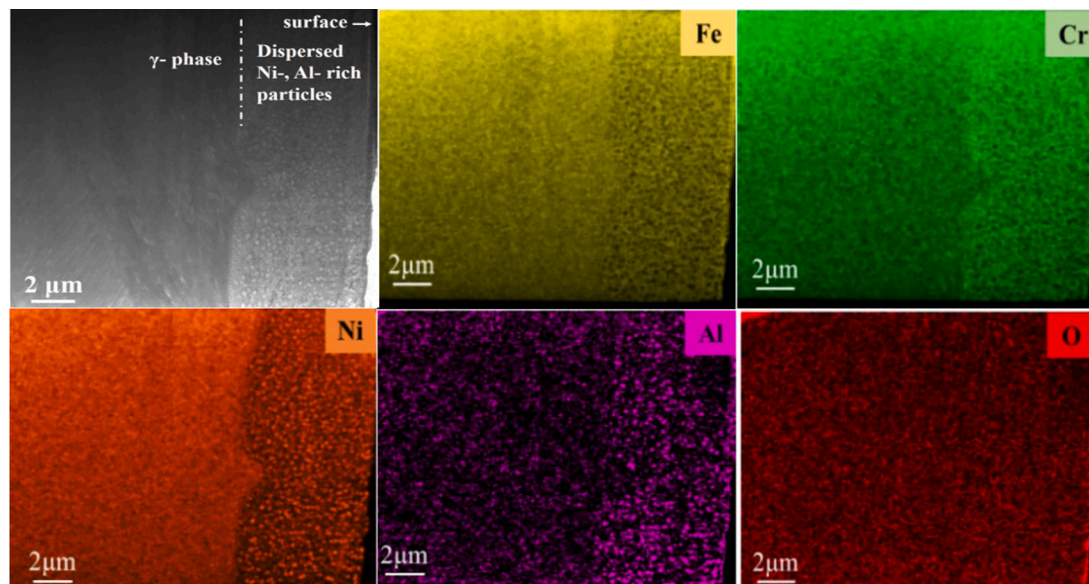
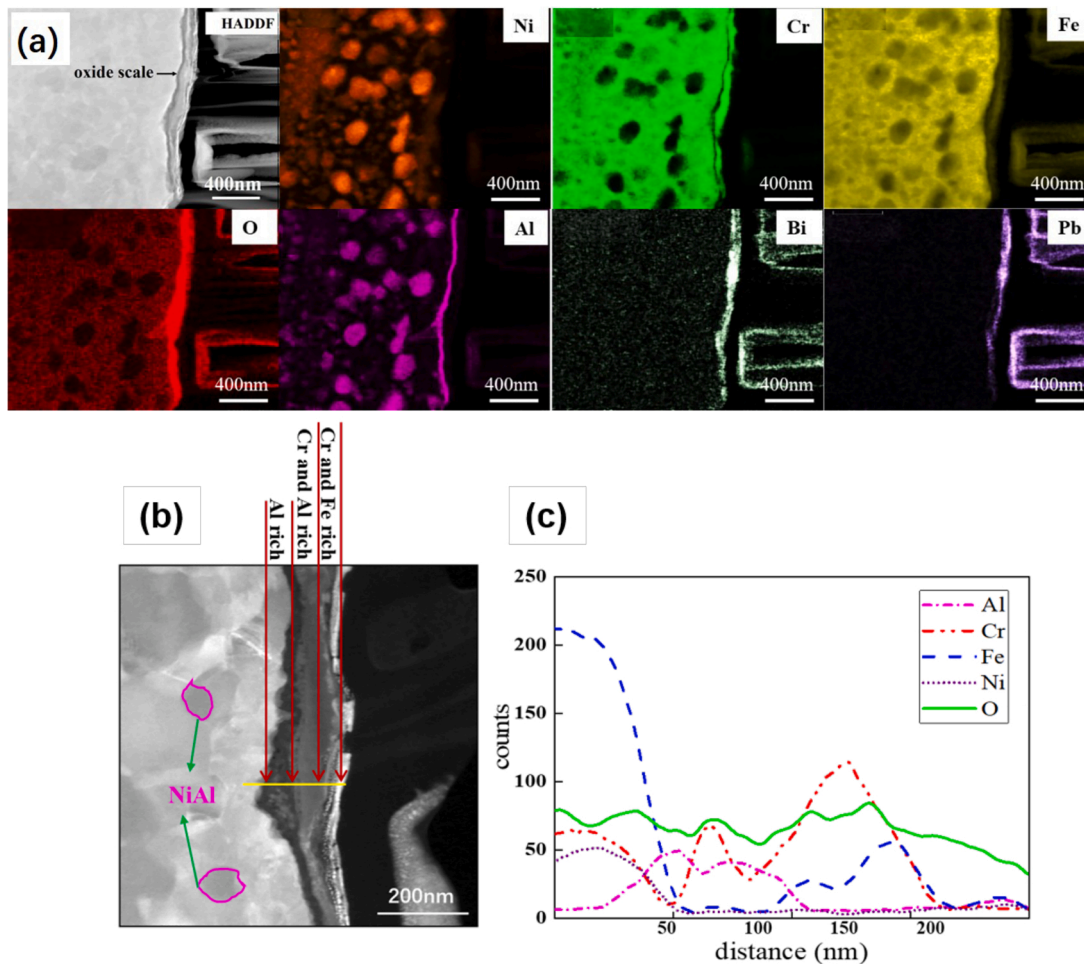**Fig. 12.** TEM/EDS elemental map immediately at the surface of D-6O.

Fig. 13. (a) TEM/EDS element mapping near the surface of the sample D-6O, (b) the thin surface layers as appearing in the TEM at high magnification as well as (c) results from EDS analyses performed along the indicated line. The distance in (c) is counted from the starting point of the line scan in the alloy.

Declaration of Competing Interest

The authors report no declarations of interest.

References

[1] S.J. Zinkle, G.S. Was, Materials challenges in nuclear energy, Acta Mater. 61 (2013) 735–758.

[2] M. Caro, K. Woloshun, F. Rubio, S.A. Maloy, P. Hosemann, Heavy liquid metal corrosion of structural materials in advanced nuclear systems, JOMUS 65 (2013) 1057–1066.

[3] J. Pacio, T. Wetzel, Assessment of liquid metal technology status and research paths for their use as efficient heat transfer fluids in solar central receiver systems, Sol. Energy 93 (2013) 11–22.

[4] Liquid Metals as Efficient High Temperature Heat Transport Fluids | Request PDF, 2017, p. 1.

[5] G. Müller, G. Schumacher, F. Zimmermann, Investigation on oxygen controlled liquid lead corrosion of surface treated steels, J. Nucl. Mater. 278 (2000) 85–95.

[6] O. Yeliseyeva, V. Tsisar, Z. Zhou, Corrosion behavior of Fe-14Cr-2W and Fe-9Cr-2W ODS steels in stagnant liquid Pb with different oxygen concentration at 550 and 650°C, J. Nucl. Mater. 442 (2013) 434–443.

[7] M. Del Giacco, A. Weisenburger, A. Jianu, F. Lang, G. Mueller, Influence of composition and microstructure on the corrosion behavior of different Fe-Cr-Al alloys in molten LBE, J. Nucl. Mater. 421 (2012) 39–46.

[8] C. Schroer, V. Tsisar, A. Durand, O. Wedemeyer, A. Skrypnik, J. Konys, Corrosion in iron and Steel T91 caused by flowing lead–bismuth eutectic at 400 °C and 10⁻⁷ mass% dissolved oxygen, J. Nucl. Eng. Radiat. Sci. 5 (2019), 011006.

[9] A. Hojna, H. Hadraba, F. Di Gabriele, R. Husak, Behaviour of pre-stressed T91 and ODS steels exposed to liquid lead-bismuth eutectic, Corros. Sci. 131 (2018) 264–277.

[10] M. Kondo, M. Takahashi, Corrosion resistance of Si- and Al-rich steels in flowing lead–bismuth, J. Nucl. Mater. 356 (2006) 203–212.

[11] C. Schroer, V. Koch, O. Wedemeyer, A. Skrypnik, J. Konys, Silicon-containing ferritic/martensitic steel after exposure to oxygen-containing flowing lead–bismuth eutectic at 450 and 550 °C, J. Nucl. Mater. 469 (2016) 162–176.

[12] A. Kimura, R. Kasada, N. Iwata, H. Kishimoto, C.H. Zhang, J. Isselin, P. Dou, J. H. Lee, N. Muthukumar, T. Okuda, M. Inoue, S. Ukai, S. Ohnuki, T. Fujisawa, T. F. Abe, Development of Al added high-Cr ODS steels for fuel cladding of next generation nuclear systems, J. Nucl. Mater. 417 (2011) 176–179.

[13] K.A. Unocic, D.T. Hoelzer, Evaluation of Pb-17Li compatibility of ODS Fe-12Cr-5Al alloys, J. Nucl. Mater. 479 (2016) 357–364.

[14] M.P. Brady, Y. Yamamoto, M.L. Santella, B.A. Pint, Effects of minor alloy additions and oxidation temperature on protective alumina scale formation in creep-resistant austenitic stainless steels, Scripta Mater. 57 (2007) 1117–1120.

[15] M.P. Brady, J. Magee, Y. Yamamoto, D. Helmick, L. Wang, Co-optimization of wrought alumina-forming austenitic stainless steel composition ranges for high-temperature creep and oxidation/corrosion resistance, Mater. Sci. Eng. A 590 (2014) 101–115.

[16] Y. Yamamoto, M.L. Santella, C.T. Liu, N.D. Evans, P.J. Maziasz, M.P. Brady, Evaluation of Mn substitution for Ni in alumina-forming austenitic stainless steels, Mater. Sci. Eng. A 524 (2009) 176–185.

[17] M.P. Brady, J. Magee, Y. Yamamoto, D. Helmick, L. Wang, Co-optimization of wrought alumina-forming austenitic stainless steel composition ranges for high-temperature creep and oxidation/corrosion resistance, Mater. Sci. Eng. A 590 (2014) 101–115.

[18] Lingzhi Chen, Zhangjian Zhou, Schroer Carsten, Research progress on compatibility of liquid metal and iron-based alloy in lead cooled energy systems, Mater. Rep. 34 (5) (2020) 5096–5101 (in Chinese).

[19] V. Tsisar, C. Schroer, O. Wedemeyer, A. Skrypnik, J. Konys, Corrosion behavior of austenitic steels 1.4970, 316L and 1.4571 in flowing LBE at 450 and 550 °C with 10^{-7} mass% dissolved oxygen, J. Nucl. Mater. 454 (2014) 332–342.

[20] A. Weisenburger, C. Schroer, A. Jianu, A. Heinzel, J. Konys, H. Steiner, G. Müller, C. Fazio, A. Gessi, S. Babayan, A. Kobzova, L. Martinelli, K. Ginestar, F. Balbaud-Célerier, F.J. Martín-Munoz, L. Soler Crespo, Long term corrosion on T91 and AISI1 316L steel in flowing lead alloy and corrosion protection barrier development: experiments and models, J. Nucl. Mater. 415 (2011) 260–269.

[21] J. Ejenstam, P. Szakálos, Long term corrosion resistance of alumina forming austenitic stainless steels in liquid lead, J. Nucl. Mater. 461 (2015) 164–170.

[22] M. Roy, L. Martinelli, K. Ginestar, J. Favergeon, G. Moulin, Dissolution and oxidation behaviour of various austenitic steels and Ni rich alloys in lead-bismuth eutectic at 520 °C, J. Nucl. Mater. 468 (2016) 153–163.

[23] M. Wang, Y. Sun, J. Feng, R. Zhang, R. Tang, Z. Zhou, Microstructural evolution and mechanical properties of an Fe-18Ni-16Cr-4Al base alloy during aging at 950°C, Int. J. Min. Metall., and Mater. 23 (2016) 314–322.

[24] C. Schroer, O. Wedemeyer, J. Konys, Aspects of minimizing steel corrosion in liquid lead-alloys by addition of oxygen, Nucl. Eng. Des. 241 (2011) 4913–4923.

[25] C. Schroer, J. Konys, Physical Chemistry of Corrosion and Oxygen Control in Liquid Lead and Lead–Bismuth Eutectic, FZKA-Report 7364, Available online at, Forschungszentrum Karlsruhe GmbH, Karlsruhe, Germany, 2007, https://pub likationen.bibliothek.kit.edu/270069895.

[26] C. Schroer, O. Wedemeyer, J. Novotny, A. Skrypnik, J. Konys, Selective leaching of nickel and chromium from Type 316 austenitic steel in oxygen-containing lead-bismuth eutectic (LBE), Corros. Sci. 84 (2014) 113–124.

[27] C. Schroer, O. Wedemeyer, J. Novotny, A. Skrypnik, J. Konys, Long-term service of austenitic steel 1.4571 as a container material for flowing lead-bismuth eutectic, J. Nucl. Mater. 418 (2011) 8–15.

[28] C. Schroer, J. Konys, Quantification of the long-term performance of steels T91 and 316L in oxygen-containing flowing lead-bismuth eutectic at 550°C, J. Eng. Gas Turbines Power 132 (2010), 082901.

[29] V. Tsisar, Z. Zhou, O. Wedemeyer, A. Skrypnik, C. Schroer, Effect of oxygen concentration in static Pb–Bi eutectic on corrosion mode of aluminum-alloyed austenitic steels at 550 °C for 1000 h, Mater. Sci. Forum 1024 (2021) 79–85.

[30] C. Schroer, A. Skrypnik, O. Wedemeyer, J. Konys, Oxidation and dissolution of iron in flowing lead-bismuth eutectic at 450°C, Corros. Sci. 61 (2012) 63–71.

[31] J. Ejenstam, M. Halvarsson, J. Weidow, B. Jonsson, P. Szakalos, Oxidation studies of Fe10CrAl-RE alloys exposed to Pb at 550°C for 10,000h, J. Nucl. Mater. 443 (2013) 161–170.

[32] A. Weisenburger, A. Jianu, S. Doyle, M. Bruns, R. Fetzer, A. Heinzel, M. DelGiacco, W. An, G. Müller, Oxide scales formed on Fe-Cr-Al-based model alloys exposed to oxygen containing molten lead, J. Nucl. Mater. 437 (2013) 282–292.

[33] C. Cionea, M.D. Abad, Y. Aussat, D. Frazer, A.J. Gubser, P. Hosemann, Oxide scale formation on 316L and FeCrAl steels exposed to oxygen controlled static LBE at temperatures up to 800°C, Sol. Energ. Mat. Sol. C 144 (2016) 235–246.

[34] M.P. Brady, Y. Yamamoto, M.L. Santella, L.R. Walker, Composition, microstructure, and water vapor effects on internal/external oxidation of alumina-forming austenitic stainless steel, Oxid. Met. 72 (2009) 311–333.

[35] M.P. Brady, K.A. Unocic, M.J. Lance, M.L. Santella, Y. Yamamoto, L.R. Walker, Increasing the upper temperature oxidation limit of alumina forming austenitic stainless steels in air with water vapor, Oxid. Met. 75 (2011) 337–357.

[36] R. Darolia, W.S. Walston, M.V. Nathal, NiAl alloys for turbine airfoils. Superalloys 1996, The minerals, Metals & Materials Society, 1996, pp. 561–570.